HIGH-SPEED LIGHT FIELD IMAGE FORMATION ANALYSIS USING WAVEFIELD MODELING WITH FLEXIBLE SAMPLING

Yanqin Chen, Xin Jin, Li Liu and Qionghai Dai

Shenzhen Key Lab of Broadband Network and Multimedia,
Graduate School at Shenzhen, Tsinghua University, Shenzhen 518055, China

ABSTRACT

Understanding the image formation inside plenoptic cameras is significant for the investigations of improving the low spatial resolution. Most researches explore the image formation from the perspective of geometric optics. However, as the hardware components in combination with low-aperture optical systems become smaller and smaller, geometric analysis will no longer be valid due to diffraction effects. In this paper, a wave-optic-based model is proposed that uses the Fresnel diffraction equation to propagate the whole object field into the plenoptic systems. The proposed model employs averaging of intensities on the sensor from uncorrelated coherent wave to avoid interference during propagations among the optical component planes. Besides, by utilizing the method of multiple partial propagations, the proposed model is much flexible at sampling on propagation planes. In order to verify the effectiveness of the proposed model, numerical simulations are conducted by comparing with existing wave optic model under different optical configurations of plenoptic cameras. Results demonstrate that the proposed model can describe the light field image formation properly. In addition, the time ratio for image formation has dropped to one in 19.22 on average by using the proposed model.

Index Terms— Plenoptic cameras, image formation, wave optics, Fresnel diffraction equation, multiple partial propagations

1. INTRODUCTION

Light field cameras, also known as plenoptic cameras, have attracted an increasing interest in recent years after Ng introduced the first prototype and processing algorithms in [1]. With the aid of inserting a microlens array (MLA) between the main lens and traditional image sensor, plenoptic cameras possess the ability to record 4D data that enable refocusing [1], depth estimations [2-3], and saliency detection [4], etc. Afterwards, this plenoptic setup has been implemented in a microscope by Levoy. *et al* [5]. As the spatial resolution of sub-aperture images is determined by the number of micro lens in plenoptic cameras 1.0, known as Lytro [6], the spatial resolution is too low since the number of micro lens is typically small. In order to investigate the possibility of recovering spatial resolution, it is useful to understand the image formation inside plenoptic cameras. However, most researches like [7-10] analyzed the image formation from the perspective of geometric optics without taking into account the diffraction effects. The continuing miniaturization of hardware components in combination with low-aperture optical systems will lead to the invalidity of geometric analysis.

Considering the effects of diffraction play important roles in plenoptic camera's design and performance, it is more accurate to analyze the image formation using wave optics. Shroff and Berkner [11] provided detailed field propagation analysis to develop a forward image formation model for plenoptic cameras 1.0 and utilized a reconstruction method that allowed the recovery of the object information beyond the resolution limit. Helin *et al* [12] and Sahin *et al* [13] further extended the wave optic model proposed in [11] for better object information recovery. Since incoherent imaging cases are generally considered in plenoptic cameras 1.0 system, this wave optic model needs to propagate the object field point by point into the system to obtain the individual impulse response on the sensor. The intensities of all impulse responses are then accumulated together to satisfy the incoherent imaging. Therefore, this solution requires much more time to obtain a complete incoherent result.

For the purpose of reducing the image formation time, this paper presents a wave optic model that propagates the whole object field into plenoptic cameras 1.0 system instead of point by point using the Fresnel diffraction equation [14]. Also, the coherence interference during propagation has been solved by employing the average of intensities on the sensor from uncorrelated coherent wave [15] to produce incoherent results. Besides, the proposed model adopts the method of multiple partial propagations [16] to relax the sampling constraints among the propagation planes. Numerical simulation results demonstrate that the light field image formation can be described properly using the proposed model. In addition, compared with the wave optic model proposed in [11], the proposed model has dropped the image formation time to one in 19.22 on average.

The rest of the paper is organized as follows. Section 2 introduces the proposed wave optic model of image formation analysis for plenoptic cameras 1.0 system in detail. Numerical simulation results and analyses are provided in Section 3. Conclusions are drawn in Section 4.

2. INCOHERENT IMAGE FORMATION MODEL

Figure 1 illustrates the schematic layout of a general plenoptic camera 1.0 system. (ξ, η), (u, v), (x, y) and (s, t) denote the spatial coordinates of object plane, main lens plane, MLA plane and sensor plane, respectively. The distances among the optical component planes satisfy the Gaussian equation [11-13], which are given by

$$\frac{1}{z_1} + \frac{1}{z_2} = \frac{1}{F_{main}} \, , \, \frac{1}{z_2} + \frac{1}{z_3} = \frac{1}{f_{MLA}}, \qquad (1)$$

where F_{main} and f_{MLA} represent the focal length of main lens and MLA, respectively.
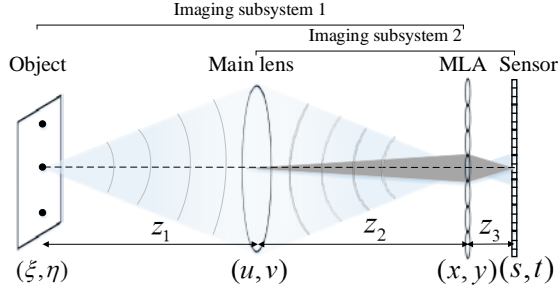

Fig. 1. Schematic layout of a plenoptic camera 1.0 system, with the imaging subsystem 1 containing the main lens (light white) and imaging subsystem 2 (gray) containing the MLA [11,17].

Wave analysis is performed in [11] to analyze the optical layout shown in Fig. 1. In the formulas, paraxial approximation is exploited and lenses are assumed to be thin and aberration-free. According to [11], the intensity at the sensor plane is given by

$$I_1(s,t) = \iint d\xi' d\eta' I_0\left(\frac{\xi'}{M_1}, \frac{\eta'}{M_1}\right) \left| \frac{e^{ikz_1} e^{ikz_2} e^{ikz_3}}{i\lambda z_3 M_1} \exp\left[\frac{ik}{2z_3}\left(s^2 + t^2\right)\right] \right.$$

$$\times \sum_m \sum_n \exp\left\{-\frac{ik}{2f_{micro}}\left[(md_1)^2 + (nd_1)^2\right]\right\}$$

$$\times \iint dxdy P(x - md_1, y - nd_1) \exp\left[\frac{ik}{2}\left(\frac{1}{z_2} + \frac{1}{z_3} - \frac{1}{f_{micro}}\right)(x^2 + y^2)\right] \quad (2)$$

$$\times \exp\left\{-ik\left[x\left(\frac{s}{z_3} - \frac{md_1}{f_{micro}}\right) + y\left(\frac{t}{z_3} - \frac{nd_1}{f_{micro}}\right)\right]\right\} \left. h_1'(x - \xi', y - \eta')\right|^2,$$

where λ is the wavelength; k is the wavelength number and equals to $2\pi/\lambda$; M_1 is the magnification from object plane to the MLA plane and equals to $-z_2/z_1$; $\xi' = M_1\xi$ and $\eta' = M_1\eta$; $P(x,y)$ is the generalized pupil function of MLA which consists of $M \times N$ micro lenses and d_1 is the corresponding diameter of each micro lens; $h_1'(x,y)$ is defined as the Fourier transform of

$$P_1(u\lambda z_2, v\lambda z_2) \exp\left\{\frac{ik}{2}\left(\frac{1}{z_1} + \frac{1}{z_2} - \frac{1}{F_{main}}\right)\left[(u\lambda z_2)^2 + (v\lambda z_2)^2\right]\right\} \quad \text{and}$$

$P_1(u,v)$ is the generalized pupil function of main lens; $I_0(\xi,\eta)$ satisfies

$$\left\langle U_o(\xi,\eta)U_0^*(\xi,\eta)\right\rangle = I_o(\xi,\eta)\delta(\xi - \tilde{\xi}, \eta - \tilde{\eta}), \quad (3)$$

where $U_o(\xi,\eta)$ represents the object field. In order to satisfy the incoherent imaging, the object field is propagated into the plenoptic camera 1.0 system point by point to obtain the individual impulse response on the sensor, and then the intensities of all impulse responses are accumulated together to form the final result, which is surely time-consuming.

2.1. Proposed wave optic model

Considering the time cost, we propose a wave optic model that propagates the whole object field $U_o(\xi,\eta)$ to the sensor plane simultaneously. As pointed in [14], the wave field from an ideal point source is perfectly spatially coherent, and if the field from the point source is observed at two points in space, the amplitudes will

be perfectly correlated. Therefore, coherence will be a big issue in the simultaneous wave field propagation. In order to decrease the coherence, the proposed model applies random transmittance screens to the object field $U_0(\xi,\eta)$ [14-15]. The procedure is illustrated in Fig. 2.
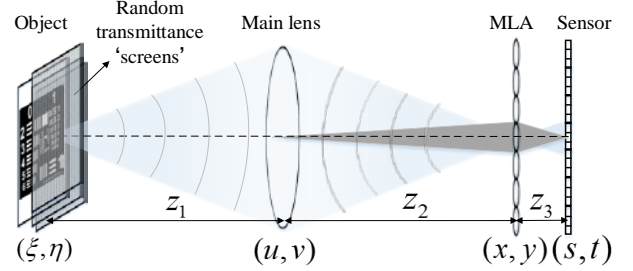

Fig. 2. Illustration of the proposed wave optic propagation model.

More specifically, the object field is now modeled as

$$U(\xi,\eta) = U_o(\xi,\eta).*\exp\left[i*2\pi*rand(\text{Num})\right], \quad (4)$$

where $rand$ function produces an $\text{Num} \times \text{Num}$ array of random values of uniform distribution over the interval [0,1] and Num denotes the number of grid spacing on the object plane. Multiplying by 2π scales the values to range over all possible phase values $[0,2\pi]$ so that every sample point has a phase that is independent and uncorrelated from every other point. Then, the new object field $U(\xi,\eta)$ propagates to main lens plane using the Fresnel propagation equation and the corresponding field on the main lens plane is described by

$$U(u,v) = \int_{-\infty}^{\infty}\int_{-\infty}^{\infty} \frac{e^{ikz_1}}{i\lambda z_1} U(\xi,\eta)\exp\left\{\frac{ik}{2z_1}\left[(\xi - u)^2 + (\eta - v)^2\right]\right\}d\xi d\eta. \quad (5)$$

After generating the field on the main lens plane, the field will pass through the main lens and arrive at the MLA plane. Similarly, the field on the MLA plane can be formulated by

$$U(x,y) = \int_{-\infty}^{\infty}\int_{-\infty}^{\infty} \frac{e^{ikz_2}}{i\lambda z_2} U'(u,v)\exp\left\{\frac{ik}{2z_2}\left[(u - x)^2 + (v - y)^2\right]\right\}dudv, \quad (6)$$

where $U'(u,v)$ is the field after traversing the main lens and is given by

$$U'(u,v) = U(u,v)P_1(u,v)\exp\left[-\frac{ik}{2F_{main}}(u^2 + v^2)\right]. \quad (7)$$

Afterwards, the field $U(x,y)$ will pass through the MLA plane, which is described by

$$U'(x,y) = U(x,y)\sum_{m\in M}\sum_{n\in N} P(x - md_1, y - nd_1)$$

$$\times \exp\left\{-\frac{ik}{2f_{MLA}}\left[(x - md_1)^2 + (y - nd_1)^2\right]\right\}. \quad (8)$$

Finally, $U'(x,y)$ reaches to the sensor plane and gives

$$U(s,t) = \int_{-\infty}^{\infty}\int_{-\infty}^{\infty} \frac{e^{ikz_3}}{i\lambda z_3} U'(x,y)\exp\left\{\frac{ik}{2z_3}\left[(x - s)^2 + (y - t)^2\right]\right\}dxdy. \quad (9)$$

Therefore, the intensity of the whole object wave field on the sensor is given by

$$I_1(s,t) = \left|U(s,t)\right|^2. \quad (10)$$

The process is repeated N_1 times with different realizations of phase and the intensities are averaged to produce the final incoherent result, which means

$$I(s,t) = \frac{1}{N_1}\sum_{j=1}^{N_1} I_j(s,t). \qquad (11)$$

2.2. Relaxed sampling with partial propagations

In order to implement numerical simulations of the above Fresnel diffraction expressions in Section 2.1, issues related to discrete sampling need to be considered. Note that the superposition integral in Eqs. (5), (6) and (9) can be written in a convolution integral. Then, the convolution theorem is used to evaluate the Fresnel diffraction expressions via two Fast Fourier Transforms (FFTs) and one inverse FFT after discretization. Take Eq. (5) as an example, the evaluation is realized as

$$U(u,v) = \mathfrak{I}^{-1}\left\{\mathfrak{I}\{U'(\xi,\eta)\}\mathfrak{I}\{h(u,v)\}\right\}, \qquad (12)$$

where $h(u,v)$ is given by

$$h(u,v) = \frac{e^{ikz_1}}{i\lambda z_1}\exp\left\{\frac{ik}{2z_1}\left(u^2 + v^2\right)\right\}. \qquad (13)$$

However, if the two-dimensional discrete convolution is simply performed to implement the numerical simulations, we will have no control over the sampling spacing in the observation plane, such as the main lens plane in imaging subsystem 1. We will be stuck with $\delta_1 = \delta_2$ where δ_1 and δ_2 are the grid spacing on the object plane and main lens plane, respectively. For fixed value of δ_2, cases like the field on the observation plane cannot be sampled adequately may happen, which will lead to aliasing on the subsequent image formation results.

For the sake of having more flexibility in selecting the grids on the observation plane, for example, the main lens plane in imaging subsystem 1, the proposed model adopts the method of multiple partial propagation provided by Schmidt [16] that introduces "*middle*" planes between the source (object) plane and the observation (main lens) plane. Instead of getting into the multiple partial propagations, two partial propagations is elaborated here, whose geometry is displayed in Fig. 3.
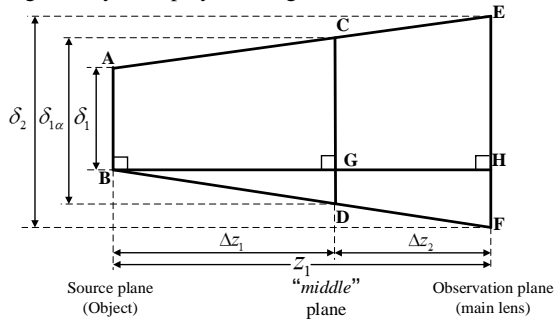

Fig. 3. Grid spacing for two partial propagations.

As shown in Fig. 3, using the similar triangle principles, we have

$$\frac{\delta_{1\alpha} - \delta_1}{2\Delta z_1} = \frac{\delta_2 - \delta_1}{2(\Delta z_1 + \Delta z_2)} = \frac{\delta_2 - \delta_1}{2z_1} = \frac{\delta_2 - \delta_{1\alpha}}{2\Delta z_2}. \qquad (14)$$

By introducing scaling parameters $\alpha = \Delta z_1 / z_1$ and $\beta = \Delta z_2 / \Delta z_1$, we can find that [14,16]

$$\delta_{1\alpha} = (1-\alpha)\delta_1 + \alpha\delta_2, \quad \delta_{1\alpha} = \frac{\lambda\Delta z_1}{\text{Num}\delta_1}, \qquad (15)$$

$$\delta_2 = \frac{\lambda\Delta z_2}{\text{Num}\delta_{1\alpha}} = \frac{\lambda\Delta z_2}{\text{Num}\left(\frac{\lambda\Delta z_1}{\text{Num}\delta_1}\right)} = \beta\delta_1. \qquad (16)$$

By denoting $\mathbf{r}_1 = \xi\mathbf{i} + \eta\mathbf{j}$ and $\mathbf{r}_2 = u\mathbf{i} + v\mathbf{j}$, equation (5) can be rewritten for simplicity as

$$U(\mathbf{r}_2) = \frac{e^{ikz_1}}{i\lambda z_1}\int_{-\infty}^{\infty} U(\mathbf{r}_1)\exp\left[\frac{ik}{2z_1}\left|\mathbf{r}_2 - \mathbf{r}_1\right|^2\right]d\mathbf{r}_1. \qquad (17)$$

Manipulating the exponential to introduce the scaling parameter β, we have

$$\begin{aligned}
\left|\mathbf{r}_2 - \mathbf{r}_1\right|^2 &= r_2^2 - 2\mathbf{r}_2\bullet\mathbf{r}_1 + r_1^2 \\
&= (r_2^2 + \frac{r_2^2}{\beta} - \frac{r_2^2}{\beta}) - 2\mathbf{r}_2\bullet\mathbf{r}_1 + (r_1^2 + \beta r_1^2 - \beta r_1^2) \\
&= \beta\left[(\frac{r_2}{\beta})^2 - 2(\frac{\mathbf{r}_2}{\beta})\bullet\mathbf{r}_1 + r_1^2\right] + (1 - \frac{1}{\beta})r_2^2 + (1-\beta)r_1^2 \\
&= \beta\left|\frac{\mathbf{r}_2}{\beta} - \mathbf{r}_1\right|^2 - (\frac{1-\beta}{\beta})r_2^2 + (1-\beta)r_1^2.
\end{aligned} \qquad (18)$$

Then, substituting Eq. (18) into Eq. (17) gives

$$U(\mathbf{r}_2) = \frac{e^{ikz_1}e^{-\frac{ik}{2z_1}\left(\frac{1-\beta}{\beta}\right)r_2^2}}{i\lambda z_1}\int_{-\infty}^{\infty}\beta U'(\mathbf{r}_1)\exp\left[\frac{ik\beta}{2z_1}\left|\frac{\mathbf{r}_2}{\beta} - \mathbf{r}_1\right|^2\right]d\mathbf{r}_1, \quad (19)$$

where $U'(\mathbf{r}_1)$ is given by

$$U'(\mathbf{r}_1) = \frac{1}{\beta}U(\mathbf{r}_1)\exp\left[\frac{ik}{2z_1}(1-\beta)r_1^2\right]. \qquad (20)$$

Then, defining the scaled coordinate and propagation distance as

$$\mathbf{r}_2' = \frac{\mathbf{r}_2}{\beta}, \quad z_1' = \frac{z_1}{\beta}, \qquad (21)$$

and substituting into Eq. (19), we have

$$U(\beta\mathbf{r}_2') = \frac{e^{ik\beta z_1'}e^{-\frac{ik}{2z_1'}(1-\beta)r_2'^2}}{i\lambda z_1'}\int_{-\infty}^{\infty} U'(\mathbf{r}_1)\exp\left[\frac{ik}{2z_1'}\left|\mathbf{r}_2' - \mathbf{r}_1\right|^2\right]d\mathbf{r}_1. \quad (22)$$

Comparing it with Eqs. (5), (6) and (9), Eq. (22) can also be described in a convolution integral form. Therefore, convolution theorem can be applied at this point and substituting back to the original coordinates allows keeping all of the details. Since the scaling parameter β is determined by the location of the "*middle*" plane, it is adjustable as the location changes. This leads to the flexibility of grid spacing on the observation (main lens) plane, as concluded from Eq. (16). It is straightforward to generalize the two partial propagations to multiple partial propagations by introducing multiple "*middle*" planes between the source (object) plane and the observation (main lens) plane. Further details can be found in [16].

3. SIMULATION RESULTS

3.1. Simulation system

To demonstrate the effectiveness of the proposed model, numerical simulations are conducted under different optical configurations of plenoptic cameras 1.0 system. The performance of the proposed model is compared with the wave optic model presented in [11]. Parameters used in the numerical simulations are summarized in Table.1. The parameters of optical components, wavelength and propagation distances in the first optical configuration are set as those in [11]. The second optical configuration makes changes in the parameters of MLA. *F-number* of main lens and MLA keeps equal for both optical configurations. In addition, both in-focus and close-to-focus cases are considered as [11].

Table.1. Parameters of two simulated imaging systems.

Parameters	Imaging system **1**	Imaging system **2**
Wavelength of light rays, λ	450nm	450nm
Focal length of main lens, F_{main}	40mm	40mm
Pupil diameter of main lens, D_1	4mm	4mm
Focal length of MLA, f_{micro}	**4mm**	**1.39mm**
Pupil diameter of microlens, d_1	**160μm**	**53.3μm**
Pixel size on the sensor	1.3μm	1.3μm
Number of grid spacing, Num	3346	3346
Propagation distance between object and main lens, z_1	64mm (close-to-focus) / 65mm (in-focus)	64mm (close-to-focus) / 65mm (in-focus)
Propagation distance between main lens and MLA, z_2	104mm	104mm
Propagation distance between MLA and sensor, z_3	**4.16mm**	**1.4mm**

3.2. Results and analysis

Numerical simulation experiments are conducted in MATLAB R2014a development environment on a PC with Intel(R) Xeon(R) CPU E5-2620 v3@2.40GHz and 64GB RAM. Figures 4(b) and (c) depict the incoherent imaging results derived from the wave optic model in [11] and the proposed model, respectively, using the parameters of imaging system **1**. Figures 5(a) and (b) depict the in-focus incoherent imaging results derived from the wave optic model in [11] and the proposed model, respectively, using the parameters of imaging system **2**, while Figs. 5(c) and (d) depict the results of close-to-focus case. The imaging results derived from the proposed model are obtained with $N_1 = 300$ and all imaging results are normalized to the same scale for display and comparison calculation. The performances are evaluated in terms of structural similarity (SSIM) and running time. SSIM is calculated by taking the results obtained from the wave optic model in [11] as the ground truth. The running time is listed in Table.2.
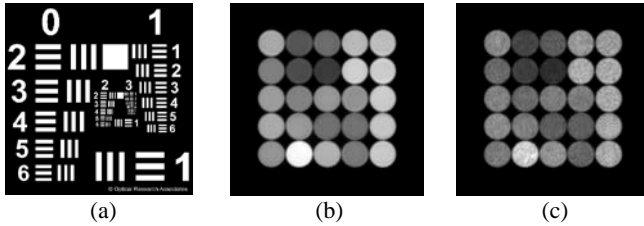

(a)   (b)   (c)

Fig. 4. Simulation results for a 5×5 array of lenslets. (a) Pristine object used in all numerical simulations; (b) Cropped plenoptic sensor data obtained by using the wave optic model in [11]; (c) Cropped plenoptic sensor data obtained by using the proposed model with SSIM=0.9280.
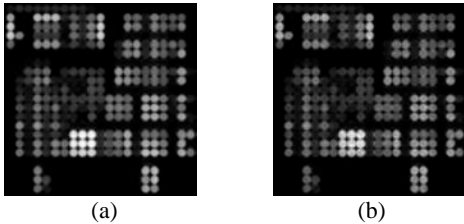

(a)   (b)

(c)   (d)

Fig. 5. Simulation results for a 23×23 array of lenslets. (a) and (c) are the in-focus and close-to-focus cropped plenoptic sensor data obtained by using the wave optic model in [11]; (b) and (d) are the corresponding cropped plenoptic sensor data obtained by using the proposed model. The SSIMs are 0.9295 and 0.9158, respectively.

Table.2. Results of running time of numerical simulations.

Simulation time (s) / Imaging system		[11]	Proposed	[11] vs. Proposed
1	$z_3 = 65mm$	333487.7	**17216.3**	19.37
2	$z_3 = 64mm$	352682.1	**18101.4**	19.48
	$z_3 = 65mm$	373896.1	**19882.7**	18.81
Average		353355.3	**18400.1**	19.22

As can be seen from Figs. 4 and 5, the proposed model can describe the light field image formation properly. The SSIMs indicate the effectiveness of the proposed model. Besides, the statistical simulation time listed in Table.2 demonstrates that the time for image formation using the proposed model is much shorter than that using the wave optic model presented in [11]. The image formation time has dropped to one in 19.22 on average, which manifests the high efficiency of the proposed model.

Although "speckle" noise exists in those plenoptic sensor data obtained from the proposed model, the noise can be reduced as N_1 increases and the "speckle" contrast falls by $1/\sqrt{N_1}$ [14-15]. According to the wave propagation analysis in Section 2, parallel processing can be applied to both kinds of models and the proposed wave optics model can be easily extended to plenoptic cameras 2.0 system, both of which are taken as our future works.

4. CONCLUSIONS

In this paper, a wave-optics-based model is proposed to analyze the light field image formation using Fresnel diffraction equations. The proposed model employs the average of intensities on the sensor from uncorrelated coherent wave to avoid the interference so that incoherent imaging results can be derived. Besides, the method of multiple partial propagations is applied to the proposed model in order to obtain flexible and adequate discrete sampling. Numerical simulation results demonstrate that the proposed model can describe the light field image formation properly and the time for image formation using the proposed model is much shorter than that using the existing wave optic model.

5. ACKNOWLEDGEMENT

6. REFERENCES

[1] R. Ng, "Digital light field photography," Ph.D dissertation, Standard, CA, USA, 2006.

[2] J.M. Tao, P. Srinivasan, J. Malik, S. Rusinkiewicz and R. Ramamoorthi, "Depth from shading, defocus, and correspondence using light-field angular coherence," in Proceedings of IEEE Conference on Computer Vision and Pattern Recognition (CVPR), pp. 1940-1948, 2015.

[3] H. Jeon, J. Park, G. Choe, J. Park, Y. Bok, Y. Tai, I. Kweon, "Accurate depth map estimation from a lenslet light field camera," in Proceedings of IEEE Conference on Computer Vision and Pattern Recognition (CVPR), pp. 1547-1555, 2015.

[4] N.Y. Li, J.W. Ye, J. Yu, H.B. Ling, and J.Y. Yu, "Saliency detection on light field", in Proceedings of IEEE Conference on Computer Vision and Pattern Recognition (CVPR), pp. 2806–2813, 2014.

[5] M. Levoy, R. Ng, A. Adams, M. Footer, and M. Horowitz, "Light field microscopy," in Proceedings of ACM SIGGRAPH, pp. 924–934, 2006.

[6] Lytro, https://www.lytro.com/.

[7] A. Lumsdaine and T. Georgiev, "Full resolution light field rendering," Technical report, Adobe Systems, 2008.

[8] T. Georgiev and A. Lumsdaine, "Superresolution with Plenoptic 2.0 cameras," in Frontiers in Optics 2009/Laser Science XXV/Fall 2009, OSA Technical Digest (CD) (Optical Society of America), paper STuA6, 2009.

[9] Raytrix, https://www.raytrix.de/.

[10] T.E. Bishop and P. Favaro, "The light field camera: extended depth of field, aliasing, and superresolution," IEEE Trans. Pattern Anal. Mach. Intell (TPAMI), 34(5), pp. 972–986, 2012.

[11] S.A. Shroff and K. Berkner, "Image formation analysis and high resolution image reconstruction for plenoptic imaging systems," Applied Optics, 52(10), pp. D22–D31, Apr. 2013.

[12] P. Helin, V. Katkovnik, A. Gotchev, and J. Astola, "Super resolution inverse imaging for plenoptic caemras using wavefield modeling," in proceedings of IEEE 3DTV Conference: The True Vision--Capture, Transmission and Display of 3D Video (3DTV-CON), pp. 1-4, 2014.

[13] E. Sahin, V. Katkovnik and A. Gotchev, "Super-resolution in a defocused plenoptic camera: a wave-optics-based approach," Optical Letters, 41(5), pp. 998-1001, Mar. 2016.

[14] D.G. Voelz, Computational fourier optics: A MATLAB Tutorial, (SPIE Tutorial Texts Vol. TT89), SPIE Press, 2011.

[15] T.A. Underwood, D.G. Voelz, "Wave optics approach for incoherent imaging simulation through distributed turbulence," in Proceedings of SPIE 8877, Unconventional Imaging and Wavefront Sensing 2013, 88770G, Sep. 2013.

[16] J.D. Schmidt, Numerical simulation of optical wave propagation with examples in MATLAB, SPIE Press, 2010.

[17] S.A. Shroff and K. Berkner, "High resolution image reconstruction for plenoptic imaging systems using system response," in Proceedings of the Computational Optical Sensing and Imaging (COSI) meeting, OSA Technical Digest (Optical Society of America, 2012), 2012.